

# Impact of Microstructure on the Electron-hole Interaction in Methylammonium Lead Iodide Perovskites

Arman Mahboubi Soufiani<sup>1</sup>, Zhuo Yang<sup>2</sup>, Trevor Young<sup>1</sup>, Atsuhiko Miyata<sup>2</sup>, Alessandro Surrente<sup>2</sup>,  
Alexander Pascoe<sup>3</sup>, Krzysztof Galkowski<sup>2,4</sup>, Roberto Brenes<sup>5</sup>, Joanna Urban<sup>2</sup>, Nan Zhang<sup>2</sup>, Vladimir  
Bulović<sup>5</sup>, Oliver Portugall<sup>2</sup>, Yi-Bing Cheng<sup>3</sup>, Robin J. Nicholas<sup>6</sup>, Anita Ho-Baillie<sup>1\*</sup>, Martin A. Green<sup>1</sup>,  
Paulina Plochocka<sup>2\*</sup>, Samuel D. Stranks<sup>5,7\*</sup>

<sup>1</sup>Australian Centre for Advanced Photovoltaics,  
School of Photovoltaic and Renewable Energy Engineering,  
University of New South Wales, Sydney, NSW 2052, Australia

<sup>2</sup>Laboratoire National des Champs Magnétiques Intenses, CNRS-UGA-UPS-INSA, 143  
Avenue de Rangueil, 31400 Toulouse, France

<sup>3</sup>Department of Materials Science and Engineering, Monash University, Clayton, Vic 3800, Australia

<sup>4</sup>Institute of Experimental Physics, University of Warsaw - Pasteura 5, 02-093 Warsaw, Poland

<sup>5</sup>Research Laboratory of Electronics, Massachusetts Institute of Technology, Cambridge, MA 02139,  
United States

<sup>6</sup>Clarendon Laboratory, University of Oxford, Parks Road, Oxford OX1 3PU, United Kingdom

<sup>7</sup>Cavendish Laboratory, University of Cambridge, J. J. Thomson Avenue, Cambridge CB3 0HE,  
United Kingdom

\*e-mail:

[a.ho-baillie@unsw.edu.au](mailto:a.ho-baillie@unsw.edu.au)

[paulina.plochocka@lncmi.cnrs.fr](mailto:paulina.plochocka@lncmi.cnrs.fr)

[sds65@cam.ac.uk](mailto:sds65@cam.ac.uk)

## Abstract

Despite the remarkable progress in the performance of devices based on the metal halide perovskite semiconductor family, there is still a lack of consensus on their fundamental photophysical properties. Here, using magneto-optical transmission spectroscopy we elucidate the impact of the microstructure on the Coulomb interaction between photo-created electron-

hole pairs in methylammonium lead triiodide ( $\text{CH}_3\text{NH}_3\text{PbI}_3$ ) by investigating thin films with a wide range of grain sizes from tens of nanometers to microns. At low temperatures in which thermal fluctuations of the interactions are frozen and the rotational disorder of the organic cation is negligible, the excitonic binding energy and reduced effective mass of carriers remain effectively unchanged with grain size. We conclude that the microstructure plays a negligible role in the Coulomb interaction of the photo-excited electron-hole pairs, in contrast to previous reports. This renewed understanding of the relationship between these fundamental electronic properties and the microstructure is critical for future fundamental studies and improving device design.

*Key words:* hybrid perovskites, microstructure, exciton binding energy, excitonic reduced effective mass, magneto-optical spectroscopy

Broader context:

Metal halide perovskites such as methylammonium lead iodide ( $\text{CH}_3\text{NH}_3\text{PbI}_3$ ) are creating enormous excitement for their use in high-performance solar cells with potential for exceptionally low capital-intensity for production. An important parameter that dictates the design of a solar cell is the strength of the Coulomb interaction between the photo-generated electron in the conduction band and the hole in the valence band (i.e. the exciton binding energy). Recently, it has been suggested that the exciton binding energy of the perovskite material is influenced by the size of the grains of the perovskite film, and therefore different device design will be required depending on the grain size. Here, we perform magneto-optic measurements on films with different grain sizes to directly show that the microstructure has a negligible influence on the excitonic properties in the films, and that excitons do not play a significant role in films with any of the polycrystalline morphologies studied. This means that excitons need not be a factor for the design of optoelectronic devices based on polycrystalline

CH<sub>3</sub>NH<sub>3</sub>PbI<sub>3</sub> and similar materials with different grain sizes, making future device architecture optimisation less constrained.

## Introduction

Solar cells based on lead halide perovskites (with general chemical formula of ABX<sub>3</sub>; A = CH<sub>3</sub>NH<sub>3</sub><sup>+</sup>, HC(NH<sub>2</sub>)<sub>2</sub><sup>+</sup> or Cs<sup>+</sup>; B = Pb<sup>2+</sup>; X = I<sup>-</sup>, Br<sup>-</sup> or Cl<sup>-</sup>) have achieved astonishingly high power conversion efficiencies exceeding 22% in only seven years since they were first used as sensitizers in photovoltaic solar cells<sup>1-3</sup>. Since then, the remarkable properties of these crystalline semiconductors, such as the tunability of their optoelectronic properties through fabrication of layers with different morphologies, compositions and crystal qualities<sup>4-7</sup>, have been further exploited to develop a variety of promising optoelectronic devices<sup>8-11</sup>.

As for any emerging semiconductor material deployable in optoelectronic devices, the strength of the Coulomb interaction between the photo-generated electron in the conduction band and the hole in the valence band is of high importance. This was a focus of several studies on perovskites about two decades ago<sup>12-14</sup> and has recently regained attention<sup>15-18</sup> mainly due to the promising outlook of perovskites for solar photovoltaics<sup>10</sup>, light-emitting diodes<sup>11</sup> and lasing applications<sup>19</sup> with polycrystalline thin films and single crystals of superior quality than those synthesized two decades ago.

The latest studies have come to a consensus that the exciton binding energy – alternatively known as effective Rydberg ( $Ry^*$ ) in the Wannier-Mott exciton model – of well-studied CH<sub>3</sub>NH<sub>3</sub>PbI<sub>3</sub> and CH<sub>3</sub>NH<sub>3</sub>PbBr<sub>3</sub> polycrystalline thin films is of the order of 5-12 meV<sup>15, 17, 18</sup> and 15-30 meV<sup>16, 18</sup> in the room and low temperature phase, respectively. These low values, with respect to thermal energy at room temperature (~ 26 meV), are due to generally weak many-body effects (i.e. Coulombic interactions) in these semiconductor systems<sup>20</sup>.

Nevertheless, there is ongoing debate concerning the possible tunability of this parameter with variations of the microstructure and hence crystal quality of the perovskite layer<sup>21, 22</sup>, being speculated to influence the photo-excited exciton binding energies.

It has been proposed that disordered organic cation dipole domains in small and defective crystals with a large portion of poly-crystallinity can create a large electrostatic potential fluctuation which causes a substantial screening of the photo-generated excitons<sup>22</sup>. This could lead to a very small value of  $Ry^*$  on the order of  $\sim 2-5$  meV<sup>23, 24</sup> meaning that the material behaves as if in the non-excitonic regime. On the other hand, large and defect-free crystals can exhibit an order of magnitude greater values of  $Ry^*$ <sup>22, 25</sup>. As a result, one current hypothesis is that it is not possible to assign a universal value to the exciton binding energy of the commonly used  $CH_3NH_3PbI_3$  and  $CH_3NH_3PbBr_3$  hybrid lead halide perovskites.

A key consequence of this could be a change in the working regime (i.e. photo-excited carrier dissociation and transport) of solar cells fabricated from active layers with diverse microstructures; in the large  $Ry^*$  regime additional mechanisms for charge carriers separation may then be required. This highlights the need to fully understand the exciton-morphology relationship. Here, we elucidate the influence of the microstructure, manipulated through the perovskite fabrication method, on the exciton binding energy  $Ry^*$  and the excitonic reduced mass ( $\mu$ ) for a variety of  $CH_3NH_3PbI_3$  crystal sizes covering the size range reported in devices to date. The impact of the local order and the degree of poly-crystallinity on electron-hole interaction is unraveled through a direct measurement of  $Ry^*$  and  $\mu^*$  for thin films with different grain sizes. These measurements are performed at low temperature (2 K) at which the impact of  $CH_3NH_3^+$  thermal orientational dynamic rearrangement is mitigated. We provide strong evidence that the grain size has negligible influence on the exciton binding energy and effective mass in  $CH_3NH_3PbI_3$  and, thus, does not affect the dissociation

probability of the bulk excitons and their stability in the photo-excited charge carrier population.

## Results and Discussion

### *Morphology and Photoluminescence Spectroscopy*

A wide range of fabrication methods, from single-step<sup>26</sup> to sequential deposition<sup>27</sup> and solution processed<sup>28</sup> to vapor-assisted<sup>29</sup> techniques, have been reported in the literature employed to fabricate the active layer of perovskite optoelectronic devices. Here, different deposition methods, which have been shown to give corresponding high-performance solar cells with efficiencies of >16 %<sup>6, 30, 31</sup>, are used to controllably tune the perovskite grain size in the films. These samples with CH<sub>3</sub>NH<sub>3</sub>PbI<sub>3</sub> chemical composition but fabricated via different methods with various resulting morphologies simulate the range of different degrees of structural disorder and poly-crystallinity in the CH<sub>3</sub>NH<sub>3</sub>PbI<sub>3</sub> layer in high-performance perovskite devices fabricated to date<sup>22</sup>. The top-view scanning electron microscope (SEM) images of the samples are presented in **Figure 1A-D**. The morphologies vary from a planar polycrystalline film with grain sizes of 772±227 nm<sup>31</sup> (**A**; large grain polycrystalline annotated **LPC**) and polycrystalline film with grain sizes of 214±57 nm<sup>30</sup> (**B**; small grain polycrystalline annotated **SPC**), to small crystals of 291±64 nm fabricated by a two-step dipping technique<sup>6</sup> (**C**; annotated **SC**) and also perovskite infiltrated into a ~2 μm thick mesoporous Aluminum oxide scaffold (mp-Al<sub>2</sub>O<sub>3</sub>) with grain sizes of <50 nm (**D**; annotated **MP**). As can be seen in the top-view SEM image of the **MP** sample, there is no visible capping layer formed on top of the mesoscopic phase and, therefore, a potential artefact from the larger grain sizes of a capping layer does not influence the related data analysis.

The optical responses of these samples were first characterized by temperature-dependent photoluminescence (PL) measurements (see **Figure 1E-H** for the complete set of spectra). A

clear difference between the luminescence behavior (i.e. peak emission position and spectral broadening) is observed for films with different grain size. The  $\text{CH}_3\text{NH}_3\text{PbI}_3$  infiltrated into the mp- $\text{Al}_2\text{O}_3$  shows the lowest peak emission wavelength and a large spectral broadening of the main excitonic peak emission at all the temperatures measured in both the orthorhombic and tetragonal phases (see Supplementary Information **Figure S1** for room temperature). Moving to the films with larger grain size, a red-shift in the PL emission is observed with respect to the **MP** sample at room temperature. This is possibly due to the less strained crystal structure of the larger grain samples <sup>6</sup>. Furthermore, it can be seen in **Figure 1E-H** that the tetragonal-to-orthorhombic phase transition temperature does not occur consistently among the investigated samples with different grain sizes, commonly reported to be at about 160 K <sup>25, 32</sup>. We note a peculiarity that this phase transition seemingly happens at higher (lower) temperatures than 160 K for the **LPC (MP)** sample, though its further investigation is beyond the scope of this study.

The contribution of the low-energy peak (at <1600 meV) luminescence intensity from the retained tetragonal phase <sup>33, 34</sup> to the overall low-temperature PL spectra varies with the morphology. While the high-energy peak (located at >1600 meV) emission of the orthorhombic phase is dominant at 4 K in the **LPC** sample, no signature of this emission can be observed in the **MP** sample; **SPC** and **SC** morphologies demonstrate contributions from both phases at low temperatures. These results highlight the vast differences between the samples in terms of morphology, structural phase transition and emission properties.

#### ***Magneto-optical Transmission Measurements***

Studying the optical behavior of excitons under external fields has proven to be a powerful tool to reveal properties of these quasi-particles in semiconductors <sup>35</sup>. Here, optical transmission measurements were conducted under high magnetic fields ( $B$ ) up to 150T on the samples presented in **Figure 1**. Typical transmission spectra for the large grain polycrystalline

thin film sample showing the strong 1S excitonic transition are given in **Figure 2A**. For unambiguous identification of the weak optical transitions, we show in **Figure 2B** the ratio of the transmission spectrum at a specific high magnetic field over the transmission spectrum taken at zero field, illustrating the free-carrier transitions. The related spectra for other morphologies are provided in the Supplementary Information, **Figure S2-S4**.

We note that a hydrogen-like excitonic behavior<sup>36</sup> can be assumed for CH<sub>3</sub>NH<sub>3</sub>PbI<sub>3</sub> in the low-temperature orthorhombic phase. The strong minimum in the transmission spectra (**Figure 2A**) is attributed to the 1S state of the hydrogen-like free exciton<sup>17</sup>, which blue shifts with increase of the magnetic field. The second minimum, located at slightly higher energies than the 1S state, is attributed to the first excitonic excited state (labelled as 2S in **Figure 2A**) and also exhibits a blue-shift with magnetic field.

The Landau levels, the free carrier states with quantum numbers  $N=0,1,2,\dots$  formed by quantization of the particle's motion in the plane perpendicular to the magnetic field<sup>35</sup>, can be observed at higher energies in the strong magnetic field regime, where  $\hbar\omega_c \gg Ry^*$  ( $\hbar\omega_c = \hbar eB/\mu$ ), where  $\hbar$  and  $e$  are Planck's constant and the electron charge, respectively. The Landau levels at high quantum numbers and magnetic fields can be fitted by  $E(B) = E_g + (N + 1/2)\hbar\omega_c$ <sup>16, 17</sup> which allows us to extract an important fundamental electronic property, namely the reduced mass,  $\mu$ , independent of the exciton binding energy.

The complete set of these excitonic and free carrier transition energies for the **LPC** sample is plotted in the fan diagram in **Figure 2D**. Knowledge of the reduced mass imposes strong constraints on fitting the excitonic binding energy. An influential constraint on the value of the binding energy is set if the higher excitonic resonances are resolved, as for the **LPC** morphology. A simultaneous global numerical fit to the hydrogen-like excitonic (dashed

lines) and free carrier (solid lines) transitions, as explained in detail in refs. <sup>16, 17, 37</sup>, is presented in **Figure 2D** and the  $Ry^*$  and  $\mu$  values for the **LPC** sample are calculated to be  $16\pm 1$  meV and  $0.102\pm 0.002m_0$ , respectively.

For the morphologies other than **LPC** (i.e. **SPC**, **SC** and **MP**), the identification of free carrier transitions at high energies allows us to obtain the values of the reduced masses. The extracted  $\mu$  values are presented in **Table 1** and are very close to the value originally reported by Miyata *et al.* ( $\mu = 0.104\pm 0.003m_0$ ) <sup>17</sup>. Importantly, we find that the microstructure has negligible influence on the reduced mass. This indicates that the polaron coupling constant, incorporating the effective longitudinal optical (LO) phonon energy and the optical and static dielectric constants of the medium, which couples to the band-edge bare effective masses to form the polaronic masses <sup>18, 38</sup>, is only minimally influenced by the variation in microstructure.

In the absence of a clear observation of the 2S excitonic transitions for the **SPC**, **SC** and **MP** samples, the global fit to the full excitonic and free-carrier transitions was employed and the resulting unchanged  $Ry^*$  values are presented in **Table 1**. To visualize the negligible change in the optical response under external magnetic fields of the  $CH_3NH_3PbI_3$  films with different morphology, the overlaid fan diagrams of the complete set of excitonic and free carrier optical transitions after shifting by the corresponding bandgap offsets are presented in **Figure 3(A)**. Here we clearly show that these  $CH_3NH_3PbI_3$  samples, although composed of dramatically different grain sizes and morphologies, exhibit similar magneto-optical behaviour. We note that, although the changes in the grain size and morphology do not influence the low temperature excitonic properties of perovskites, they can affect the optoelectronic response of these materials including their PL behaviour, phase transition temperature and the fraction of retained tetragonal phase within the orthorhombic phase upon lowering the temperature (see **Figure 1E-H**) <sup>33, 34, 39</sup>.



It was recently shown that when replacing  $\text{CH}_3\text{NH}_3^+$  by a larger monovalent organic cation, formamidinium ( $\text{HC}(\text{NH}_2)_2^+$ ), the excitonic characteristics of the corresponding perovskite,  $Ry^*$  and  $\mu$ , decreased by less than 15 %<sup>16</sup>. The larger steric size of formamidinium compared to methylammonium results in a larger equatorial bond angle (lead-iodide-lead) and thus, a narrower optical bandgap<sup>40</sup>. The variation of the crystal size would result in a modified interplay between the organic and the inorganic moieties in the perovskite structure, which in turn changes the strain induced on the crystal structure and thus, impacts the bandgap. The negligible impact on the excitonic characteristics of the degree of dipolar cation order and structural arrangement induced by the variation of perovskite microstructure might be analogous to the small impact of cation substitution on the excitonic properties, with the lead-halogen sub-unit remaining unchanged in both cases. This indeed demonstrates the critical role of the electronic properties of the inorganic cage in the determination of the excitonic binding energy and reduced effective mass of perovskites. Moreover, this important observation agrees with the recent work by Perez-Osorio *et al.* in which the largest contribution to the static dielectric constant of  $\text{CH}_3\text{NH}_3\text{PbI}_3$  was demonstrated to originate from the stretching and rocking vibrational modes of the lead-halogen system rather than the internal modes of the organic cation<sup>41</sup>.

Using the values obtained for the effective dielectric constant ( $\varepsilon = \sqrt{Ry^H \times \mu / Ry^* \times m_0}$ , where  $Ry^H = 13.6$  eV is the Rydberg constant of the hydrogen atom) and the reduced mass, the Bohr radius of the bound electron-hole system can be calculated. This is similar for all the perovskite morphologies and is about 5 nm in the low temperature phase. The Bohr radius is substantially smaller even than the perovskite crystal size of the **MP** sample and it is consistent with the absence of any signature of a quantum confinement effect on the optical transition of the corresponding excitons in the mesoscopic phase.

The correct interpretation of the optical absorption spectrum for the exciton binding energy derivation in the room temperature tetragonal phase ( $> 160$  K) becomes more difficult than in the orthorhombic phase as the large spectral broadening at higher temperatures in the tetragonal phase can potentially mask critical optical transition features even under high magnetic fields<sup>17</sup>. The increased broadening is most likely due to a thermally-induced increase in the orientational disorder and rotational dynamics of the unlocked organic cation above the structural phase transition<sup>42</sup>. The excitonic binding energy has been reported in the literature<sup>17, 18, 24, 43</sup> to decrease upon orthorhombic-to-tetragonal phase transition with a likely reason to be the slight increase in the medium dielectric constant, which is in turn linked to the increase in the effective phonon energy coupling to the carriers.

We argue that the change in the binding energy at the transition to the tetragonal phase for all the morphologies investigated in this study would be similar. This can be partly understood by the dominant influence of thermal disorder on the electrostatic fluctuations at room temperature over the degree of poly-crystallinity and molecular order which are dominant at lower temperatures<sup>22</sup>; the latter properties we have already shown above to have insignificant impact on the electron-hole interaction. This is further supported by a recent theoretical study by Motta *et al.* in which the impact of the degree of molecular dipole orientational disorder – which could be induced by the grain size variation – on the binding energy in the high temperature phase of  $\text{CH}_3\text{NH}_3\text{PbI}_3$  was found to be only about 10 %<sup>44</sup>.

Recently, Petrozza and co-workers used temperature-dependent time-resolved transient absorption (TA) spectroscopy to track the fate of excitons following photo-excitation and to understand the relationship between the excitonic properties and film morphology<sup>22</sup>. The conclusion from this study was that the exciton binding energy and, therefore, exciton stability can vary depending on the perovskite film microstructure in the tetragonal phase which is most critical to solar cell operation. Their interpretation was based on the emergence

and evolution of the negative feature located at the high-energy end of the photobleach signature in the transmission-difference spectrum, which was attributed to self-renormalization of the exciton energy due to a change in its concentration upon decrease in temperature and/or grain size variation. We note that the negative feature developing in the high-energy tail of the TA spectra over time has been proposed to be primarily a consequence of a bandgap renormalization effect (bandgap narrowing) and of a free carrier absorption, among other possible mechanisms<sup>45, 46</sup>. The spectral TA analysis used in ref.<sup>22</sup>, which is an indirect technique for characterising excitonic properties, can also be influenced by recombination mechanisms which are strongly influenced by the perovskite crystal morphology. Furthermore, we note from a previous report for CH<sub>3</sub>NH<sub>3</sub>PbBr<sub>3</sub> perovskite that while  $R_y^*$  probably remains unchanged by increasing the temperature from 2 K to room temperature, the increase in the broadening of the linear absorption spectra lessens the 1S transition strength<sup>18, 47</sup>. Although this spectral broadening increase is mainly attributed to thermally activated mechanisms, a change in the intrinsic broadening of perovskites with different microstructures (see linewidth values extracted from spectral PL measurements in Supplementary Information **Figure S1**), due for instance to the difference in their inherent structural disorder, can similarly influence the spectral shape while  $R_y^*$  remains unchanged. This makes unambiguous interpretation of the linear and transient absorption spectra difficult when relying on the detection of the excitonic feature – at the absorption edge – as these techniques are indirect approaches for  $R_y^*$  determination compared to the direct approach employed in this study.

## Conclusions

The relationship between the excitonic properties and microstructure of the CH<sub>3</sub>NH<sub>3</sub>PbI<sub>3</sub> perovskite was investigated using magneto-optical spectroscopy measurements. The microstructure does not influence the excitonic binding energy of CH<sub>3</sub>NH<sub>3</sub>PbI<sub>3</sub>. Thus, we

conclude that excitons truly play a negligible role in the operation of organic cation-based perovskites regardless of the thin film deposition technique and final morphology, and that excitons need not be a factor for the design of optoelectronic devices based on polycrystalline  $\text{CH}_3\text{NH}_3\text{PbI}_3$  and similar materials with different grain sizes. The universal values of 16 meV and  $0.102\text{--}0.109m_0$  measured for the exciton binding energy and reduced effective mass in the low temperature phase can be used as guidelines for interpretation of the spectroscopic data such as the complex spectra of transient absorption measurements. It also implies that the electronic structure of the inorganic  $(\text{PbI}_3)^-$  cage is likely to have the greatest contribution to the excitonic properties of organic-inorganic lead halide perovskites rather than the degree of poly-crystallinity and the order of dipolar organic cation domains.

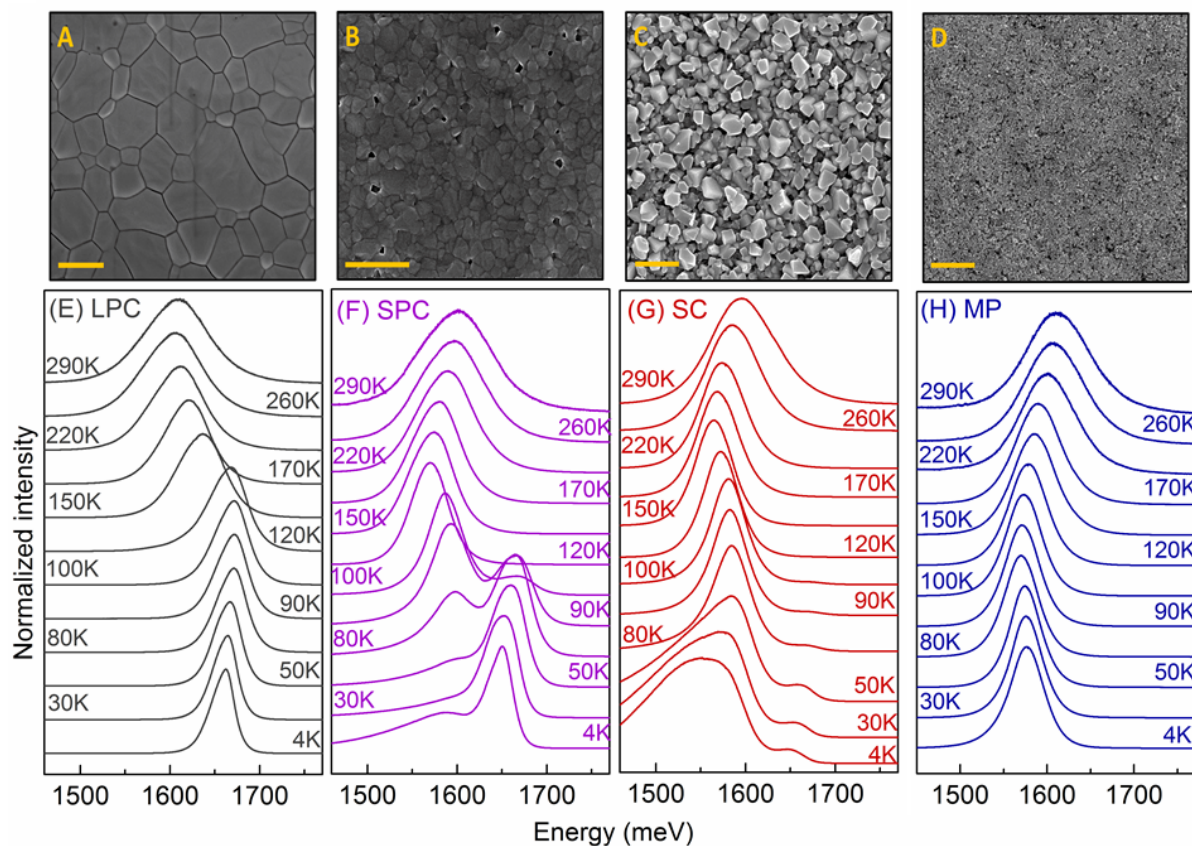


**Figure 1 Morphology of  $\text{CH}_3\text{NH}_3\text{PbI}_3$  samples.** Top-view SEM images of  $\text{CH}_3\text{NH}_3\text{PbI}_3$  layer with various morphologies fabricated on glass substrates. **A)** Polycrystalline thin film with grain sizes  $772 \pm 227$  nm (LPC). **B)** Polycrystalline thin film with grain sizes  $214 \pm 57$  nm (SPC). **C)** Small crystals of  $\text{CH}_3\text{NH}_3\text{PbI}_3$  fabricated by the two-step solution-processed dipping technique, with resulting crystal sizes  $291 \pm 64$  nm (SC). **D)**  $\text{CH}_3\text{NH}_3\text{PbI}_3$  infiltrated into a thick mesoporous- $\text{Al}_2\text{O}_3$  scaffold with grain sizes  $< 50$  nm (MP). Scale bars are 1  $\mu\text{m}$ . Panels **(E-H)** show the temperature-dependent photoluminescence data associated with the large grain polycrystalline **(E)**, small grain polycrystalline **(F)**, small crystal **(G)** and mp- $\text{Al}_2\text{O}_3$  infiltrated **(H)**  $\text{CH}_3\text{NH}_3\text{PbI}_3$  samples. Samples were photo-excited with a 532-nm CW laser.

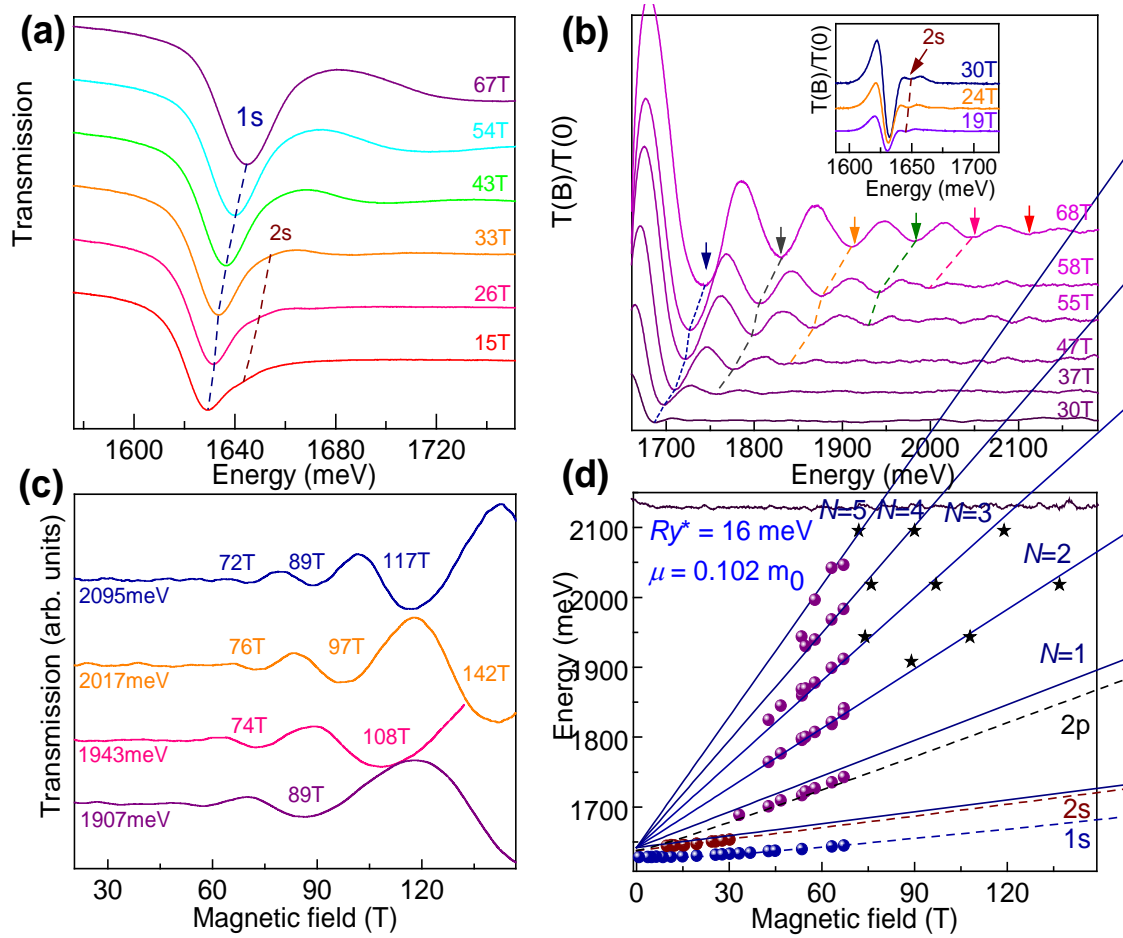


**Figure 2 Magneto-optical transmission spectrum and fan chart measured at 2 K.** **A)** Sequence of typical optical transmission spectra of the **LPC** sample measured at the indicated magnetic fields which show the 1S and 2S excitonic transitions with increased transmission. **B)** Sequences of the ratios of the transmission spectra in magnetic field  $T(B)$  to that measured at zero field  $T(0)$ . The resonant absorption features of the free carrier Landau levels correspond to minima. **C)** Typical results of the low temperature monochromatic transmission as a function of magnetic field obtained by the short pulse technique. **D)** Fan chart of  $\text{CH}_3\text{NH}_3\text{PbI}_3$  for the large grain polycrystalline sample. The circular data points are from long pulse field measurements and star symbol points are collected by short pulse mega-gauss measurements. The solid lines and the dashed lines are the fits to the set of Landau levels and the excitonic transitions, respectively.

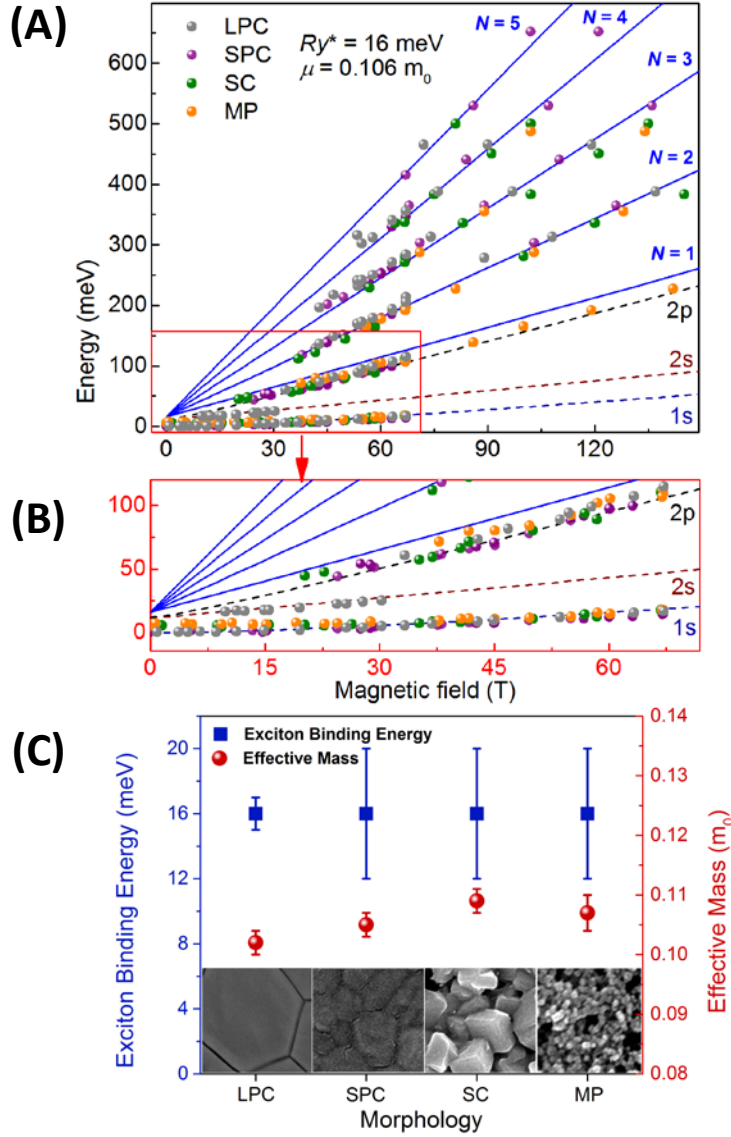


**Figure 3 Comparison of the excitonic properties of the four different  $\text{CH}_3\text{NH}_3\text{PbI}_3$  morphologies. A)** Overlaid fan chart of the LPC, SPC, SC and MP samples. The solid lines and the dashed lines are the fits to the set of Landau levels and the excitonic transitions, respectively. **B)** The zoomed-in plot of the excitonic transitions region of the fan chart in panel (A). **C)** The bottom panel illustrates the change in the  $Ry^*$  and  $\mu$  for the various morphologies.

**Table 1** Summary of the parameters of the fits to the full Landau fan chart for the four different morphologies of  $\text{CH}_3\text{NH}_3\text{PbI}_3$  in the low temperature (2 K), orthorhombic phases. The figures in the brackets are the error estimates of the parameters.

	<b>Size Distribution (nm)</b>	$E_g$ (meV)	$\mu$ ( $m_0$ )	$Ry^*$ (meV)
<b>Large Polycrystalline</b>	772(227)	1642(2)	0.102(0.002)	16(1)
<b>Small Polycrystalline</b>	214(57)	1643(2)	0.105(0.002)	16(4)
<b>Small Crystal</b>	291(64)	1639(2)	0.109(0.002)	16(4)
<b>Mesoporous</b>	<50	1638(2)	0.107(0.003)	16(4)



## Acknowledgements

A.M.S. would like to thank Jincheol Kim for assisting in optimizing the two-step dipping solution-processed samples. The authors acknowledge support from the Australian Government through the Australian Renewable Energy Agency (ARENA) and the Australian Centre for Advanced Photovoltaics (ACAP). The views expressed herein are not necessarily the views of the Australian Government, and the Australian Government does not accept responsibility for any information or advice contained herein. S.D.S. acknowledges funding from the People Programme (Marie Curie Actions) of the European Union's Seventh Framework Programme (FP7/2007–2013) under REA grant agreement number PIOF-GA-2013-622630. This work was partially supported by ANR JCJC project milliPICS, the Région Midi-Pyrénées under contract MESR 13053031, BLAPHENE project under IDEX program Emergence. Zhuo Yang holds a fellowship from the Chinese Scholarship Council (CSC). This work was supported by EPSRC (UK) via its membership to the EMFL (grant no. EP/N01085X/1).

## Methods

### Sample preparation

#### *Large grain polycrystalline film (LPC)*

LPC perovskite films were prepared using a methylammonium iodide ( $\text{CH}_3\text{NH}_3\text{I}$ ) and lead acetate  $\text{Pb}(\text{Ac})_2 \cdot 3\text{H}_2\text{O}$  precursor mixture<sup>31</sup>. To generate the perovskite solution,  $\text{CH}_3\text{NH}_3\text{I}$  (Dyesol) and  $\text{Pb}(\text{Ac})_2 \cdot 3\text{H}_2\text{O}$  were dissolved in anhydrous N,N-dimethylformamide at a 3:1 molar ratio with final concentration of 30 wt%, and the stabilizer hypophosphorous acid (HPA) was added at a molar ratio of 7.5% with respect to  $\text{Pb}(\text{Ac})_2 \cdot 3\text{H}_2\text{O}$ .  $\text{Pb}(\text{Ac})_2 \cdot 3\text{H}_2\text{O}$  (316512) and HPA (214906) were purchased from Sigma Aldrich. Microscope slides and coverslips were washed sequentially with soap (2% vol. Hellmanex in water), de-ionized

water, isopropanol, acetone and finally treated under oxygen plasma for 10 min. The precursor solution was spin-coated at 2,000 r.p.m. for 45 s in a nitrogen-filled glovebox, and the substrates were then dried at room temperature for 10 min before annealing at 100 °C for 5 min. The samples were then stored in a nitrogen-filled glovebox until used.

#### ***Small grain polycrystalline film (SPC)***

Soda-lime glass substrates 1 mm thick were purchased from J. Melvin Freed. The substrates were cleaned ultrasonically using soap solution (Helmanex), water, ethanol and iso-propanol for 15 minutes, each.

PbI<sub>2</sub> (99.99%) was purchased from Alfa Aesar and used without further purification. MAI was either synthesised in-house using a common method or else purchased from Dyesol. All the film preparation work was carried out under nitrogen atmosphere.

CH<sub>3</sub>NH<sub>3</sub>PbI<sub>3</sub> films were prepared by the “gas-assisted” method of Huang *et al.*<sup>30</sup>. A 25 µL 45 wt% CH<sub>3</sub>NH<sub>3</sub>PbI<sub>3</sub> DMF solution, prepared from PbI<sub>2</sub> and CH<sub>3</sub>NH<sub>3</sub>I in a molar ratio of 1:1, was spread on the substrate, on a spin-coater. An 80 L/min stream of nitrogen gas was blown over the film during spinning at 6500 rpm, 2 s after the spinning commenced. The films were annealed at 100°C on a hotplate for 10 min and then cooled to room temperature.

#### ***Small crystal sample (SC)***

Soda-lime glass substrates treatment and precursor solution (PbI<sub>2</sub> and MAI) preparation were similar to that of the small grain polycrystalline film.

CH<sub>3</sub>NH<sub>3</sub>PbI<sub>3</sub> films were prepared by the 2-step method of D’Innocenzo *et al.*<sup>6</sup>. The clean glass substrates were heated on a hotplate at 70° C. A PbI<sub>2</sub> solution in DMF (462 mg/mL) was warmed to 70°C and then spin-coated at 2000 rpm for 60 s. The PbI<sub>2</sub> films were subsequently annealed at 70°C for 30 min. CH<sub>3</sub>NH<sub>3</sub>PbI<sub>3</sub> films with the largest grains were prepared by

dipping the  $\text{PbI}_2$ -coated substrates in a 0.031 M  $\text{CH}_3\text{NH}_3\text{I}$  solution in isopropanol at 70°C for 2 minutes.  $\text{CH}_3\text{NH}_3\text{PbI}_3$  films with intermediate grain size were prepared by dipping the  $\text{PbI}_2$ -coated substrates in a 0.063 M  $\text{CH}_3\text{NH}_3\text{I}$  solution in isopropanol at 25°C for 2 minutes. Samples were finally rinsed in anhydrous IPA to remove unreacted  $\text{CH}_3\text{NH}_3\text{I}$ .

### ***Mesoporous $\text{Al}_2\text{O}_3$ (MP)***

Unless otherwise specified, all materials were purchased from either Alfa Aesar or Sigma-Aldrich and used as received. The synthesis of  $\text{CH}_3\text{NH}_3\text{I}$  was performed using the same previously reported method<sup>30</sup>. The  $\text{Al}_2\text{O}_3$  (Aldrich, 642991) nanoparticle paste used for characterization measurements was formed by suspending ~ 45 nm particles in a solution of ethanol, terpineol and ethyl cellulose.

Glass substrates were cleaned by sonication in ethanol for 10 mins. The mesoporous  $\text{Al}_2\text{O}_3$  layer was formed by drop coating approximately 30  $\mu\text{L}/\text{cm}^2$  of the nanoparticle solution on the glass substrates, which were then annealed at 500 °C for 30 mins. The perovskite precursor solution was formed by mixing stoichiometric amounts of  $\text{CH}_3\text{NH}_3\text{I}$  and  $\text{PbI}_2$  in a combination of dimethyl sulfoxide (DMSO) and *N*-methyl-2-pyrrolidone (NMP) (7:3 vol) to form a (46 wt%) concentration solution. Approximately 30  $\mu\text{L}/\text{cm}^2$  of the perovskite precursor solution was applied to the surface of the substrate prior to spin-coating. The films were spin-coated using a two-stage process: 1000 rpm for 5 s using an acceleration of 200 rpm/s, then 6000 rpm for 50 s using an acceleration of 6000 rpm/s. A nitrogen gas flow was introduced after 20 s of the second spin-coating step and sustained for a further 20 s. The perovskite films were then annealed on a hot-plate at 100 °C for a duration of 10 mins.

### **Magneto-optical measurement**

The magneto transmission measurements were performed combining long pulse magnetic field measurements and 150 T short duration pulsed magnets.

For the long pulse measurements, the typical duration of the pulse is around 100 ms with the magnetic field up to 66 T. For these measurements, the sample was placed in a liquid helium cryostat. White light from a halogen lamp was used as the excitation source. The light emitted from the lamp was coupled in a 200  $\mu\text{m}$ -diameter multimode fiber, used to illuminate sample. The transmitted light was collected by a 400  $\mu\text{m}$ -diameter multimode fiber and guided to a spectrometer equipped with a liquid nitrogen cooled CCD camera. The typical exposure time was  $<3$  ms, which ensured that the transmission spectra were acquired at an essentially constant magnetic field value.

For very high magnetic field measurements ( $B < 150$  T), pulse having a typical duration  $< 10$   $\mu\text{s}$  were generated by a single turn coil system with a bore diameter of 10 mm. A non-conducting helium-flow cryostat was located in the single turn coil. The sample was kept at a temperature of  $\sim 5$  K. Magneto-transmission measurements were conducted by using a tunable Optical Parametric Oscillator pumped by a Ti:sapphire laser as the light source. A fast (100 MHz) silicon detector and a high speed digital oscilloscope was used for detection.

#### **Steady-state spectral photoluminescence measurement**

For the micro-PL measurement, the samples were placed in a helium flow cryostat with optical access. The cryostat was equipped with a heater which allowed setting the temperature from 4-300 K. A semiconductor laser with excitation wavelength of 532 nm was used. The microscope objective lens (50x, numerical aperture 0.55) was used to focus the laser on the sample, giving a typical spot size 1  $\mu\text{m}$ . The PL was collected from the sample with the same objective and was dispersed by a spectrometer equipped with a nitrogen-cooled CCD camera.

## 409 Reference

- 410 1. D. Bi, W. Tress, M. I. Dar, P. Gao, J. Luo, C. Renevier, K. Schenk, A. Abate, F. Giordano, J.-P.  
411 Correa Baena, J.-D. Decoppet, S. M. Zakeeruddin, M. K. Nazeeruddin, M. Grätzel and A.  
412 Hagfeldt, *Science Advances*, 2016, **2**.
- 413 2. M. Saliba, T. Matsui, J.-Y. Seo, K. Domanski, J.-P. Correa-Baena, N. Mohammad K, S. M.  
414 Zakeeruddin, W. Tress, A. Abate, A. Hagfeldt and M. Gratzel, *Energy & Environmental*  
415 *Science*, 2016, **9**, 1989-1997.
- 416 3. A. Kojima, K. Teshima, Y. Shirai and T. Miyasaka, *Journal of the American Chemical Society*,  
417 2009, **131**, 6050-6051.
- 418 4. N. J. Jeon, J. H. Noh, W. S. Yang, Y. C. Kim, S. Ryu, J. Seo and S. I. Seok, *Nature*, 2015, **517**,  
419 476-480.
- 420 5. D. P. McMeekin, G. Sadoughi, W. Rehman, G. E. Eperon, M. Saliba, M. T. Hörantner, A.  
421 Haghighirad, N. Sakai, L. Korte, B. Rech, M. B. Johnston, L. M. Herz and H. J. Snaith, *Science*,  
422 2016, **351**, 151-155.
- 423 6. V. D’Innocenzo, A. R. Srimath Kandada, M. De Bastiani, M. Gandini and A. Petrozza, *Journal of*  
424 *the American Chemical Society*, 2014, **136**, 17730-17733.
- 425 7. C. G. Bischak, E. M. Sanehira, J. T. Pecht, J. M. Luther and N. S. Ginsberg, *Nano Letters*, 2015,  
426 **15**, 4799-4807.
- 427 8. Z.-K. Tan, R. S. Moghaddam, M. L. Lai, P. Docampo, R. Higler, F. Deschler, M. Price, A.  
428 Sadhanala, L. M. Pazos, D. Credgington, F. Hanusch, T. Bein, H. J. Snaith and R. H. Friend, *Nat*  
429 *Nano*, 2014, **9**, 687-692.
- 430 9. M. Saliba, S. M. Wood, J. B. Patel, P. K. Nayak, J. Huang, J. A. Alexander-Webber, B. Wenger,  
431 S. D. Stranks, M. T. Hörantner, J. T.-W. Wang, R. J. Nicholas, L. M. Herz, M. B. Johnston, S. M.  
432 Morris, H. J. Snaith and M. K. Riede, *Advanced Materials*, 2016, **28**, 923-929.
- 433 10. M. A. Green, A. Ho-Baillie and H. J. Snaith, *Nat Photon*, 2014, **8**, 506-514.
- 434 11. S. D. Stranks and H. J. Snaith, *Nature Nanotechnology*, 2015, **10**, 391-402.
- 435 12. T. Ishihara, *Journal of Luminescence*, 1994, **60-61**, 269-274.
- 436 13. M. Hirasawa, T. Ishihara, T. Goto, K. Uchida and N. Miura, *Physica B: Condensed Matter*,  
437 1994, **201**, 427-430.
- 438 14. M. Hirasawa, T. Ishihara and T. Goto, *Journal of the Physical Society of Japan*, 1994, **63**, 3870-  
439 3879.
- 440 15. M. E. Ziffer, J. C. Mohammed and D. S. Ginger, *ACS Photonics*, 2016, **3**, 1060-1068.
- 441 16. K. Galkowski, A. Mitioglu, a. miyata, p. plochocka, o. Portugall, G. E. Eperon, J. T.-W. Wang, T.  
442 Stergiopoulos, S. D. Stranks, H. Snaith and R. J. Nicholas, *Energy & Environmental Science*,  
443 2016, **9**, 962-970.
- 444 17. A. Miyata, A. Mitioglu, P. Plochocka, O. Portugall, J. T.-W. Wang, S. D. Stranks, H. J. Snaith and  
445 R. J. Nicholas, *Nat Phys*, 2015, **11**, 582-587.
- 446 18. A. M. Soufiani, F. Huang, P. Reece, R. Sheng, A. Ho-Baillie and M. A. Green, *Applied Physics*  
447 *Letters*, 2015, **107**, 231902.
- 448 19. Y. Fu, H. Zhu, C. C. Stoumpos, Q. Ding, J. Wang, M. G. Kanatzidis, X. Zhu and S. Jin, *ACS Nano*,  
449 2016, **10**, 7963-7972.
- 450 20. S. A. March, D. B. Riley, C. Clegg, D. Webber, X. Liu, M. Dobrowolska, J. K. Furdyna, I. G. Hill  
451 and K. C. Hall, *arXiv preprint arXiv:1602.05186*, 2016.
- 452 21. A. R. Srimath Kandada and A. Petrozza, *Accounts of Chemical Research*, 2016, **49**, 536-544.
- 453 22. G. Grancini, A. R. Srimath Kandada, J. M. Frost, A. J. Barker, M. De Bastiani, M. Gandini, S.  
454 Marras, G. Lanzani, A. Walsh and A. Petrozza, *Nat Photon*, 2015, **9**, 695-701.
- 455 23. Q. Lin, A. Armin, R. C. R. Nagiri, P. L. Burn and P. Meredith, *Nature Photonics*, 2014, **9**, 106-  
456 112.
- 457 24. J. Even, L. Pedesseau and C. Katan, *The Journal of Physical Chemistry C*, 2014, **118**, 11566-  
458 11572.

25. V. D’Innocenzo, G. Grancini, M. J. P. Alcocer, A. R. S. Kandada, S. D. Stranks, M. M. Lee, G. Lanzani, H. J. Snaith and A. Petrozza, *Nat Commun*, 2014, **5**.
26. J. Kim, J. S. Yun, X. Wen, A. M. Soufiani, C. F. J. Lau, B. Wilkinson, J. Seidel, M. A. Green, S. Huang and A. W. Y. Ho-Baillie, *The Journal of Physical Chemistry C*, 2016, **120**, 11262–11267.
27. J. Burschka, N. Pellet, S.-J. Moon, R. Humphry-Baker, P. Gao, M. K. Nazeeruddin and M. Gratzel, *Nature*, 2013, **499**, 316–319.
28. W. S. Yang, J. H. Noh, N. J. Jeon, Y. C. Kim, S. Ryu, J. Seo and S. I. Seok, *Science*, 2015, **348**, 1234–1237.
29. M. Liu, M. B. Johnston and H. J. Snaith, *Nature*, 2013, **501**, 395–398.
30. F. Huang, Y. Dkhissi, W. Huang, M. Xiao, I. Benesperi, S. Rubanov, Y. Zhu, X. Lin, L. Jiang and Y. Zhou, *Nano Energy*, 2014, **10**, 10–18.
31. W. Zhang, S. Pathak, N. Sakai, T. Stergiopoulos, P. K. Nayak, N. K. Noel, A. A. Haghighirad, V. M. Burlakov, D. W. deQuilettes, A. Sadhanala, W. Li, L. Wang, D. S. Ginger, R. H. Friend and H. J. Snaith, *Nat Commun*, 2015, **6**.
32. C. Wehrenfennig, M. Liu, H. J. Snaith, M. B. Johnston and L. M. Herz, *APL Materials*, 2014, **2**, 081513–081523.
33. A. Osherov, E. M. Hutter, K. Galkowski, R. Brenes, D. K. Maude, R. J. Nicholas, P. Plochocka, V. Bulović, T. J. Savenije and S. D. Stranks, *Advanced Materials*, 2016, **28**, 10757–10763.
34. K. Galkowski, A. A. Mitioglu, A. Surrente, Z. Yang, D. K. Maude, P. Kossacki, G. E. Eperon, J. T. W. Wang, H. J. Snaith, P. Plochocka and R. J. Nicholas, *Nanoscale*, 2017, **In Press**.
35. C. F. Klingshirn, *Semiconductor optics*, Springer, 2007.
36. J. Tilchin, D. N. Dirin, G. I. Maikov, A. Sashchiuk, M. V. Kovalenko and E. Lifshitz, *ACS Nano*, 2016, **10**, 6363–6371.
37. P. C. Makado and N. C. McGill, *Journal of Physics C: Solid State Physics*, 1986, **19**, 873.
38. G. Mahan, *Proc. 1971 Antwerp Advanced Study Inst*, 1972.
39. D. Li, G. Wang, H.-C. Cheng, C.-Y. Chen, H. Wu, Y. Liu, Y. Huang and X. Duan, *Nat Commun*, 2016, **7**.
40. M. R. Filip, G. E. Eperon, H. J. Snaith and F. Giustino, *Nature communications*, 2014, **5**.
41. M. A. Pérez-Osorio, R. L. Milot, M. R. Filip, J. B. Patel, L. M. Herz, M. B. Johnston and F. Giustino, *The Journal of Physical Chemistry C*, 2015, **119**, 25703–25718.
42. A. M. A. Leguy, A. R. Goni, J. M. Frost, J. Skelton, F. Brivio, X. Rodriguez-Martinez, O. J. Weber, A. Pallipurath, M. I. Alonso, M. Campoy-Quiles, M. T. Weller, J. Nelson, A. Walsh and P. R. F. Barnes, *Physical Chemistry Chemical Physics*, 2016, **18**, 27051–27066.
43. Y. Yamada, T. Nakamura, M. Endo, A. Wakamiya and Y. Kanemitsu.
44. C. Motta, P. Mandal and S. Sanvito, *Physical Review B*, 2016, **94**, 045202.
45. M. B. Price, J. Butkus, T. C. Jellicoe, A. Sadhanala, A. Briane, J. E. Halpert, K. Broch, J. M. Hodgkiss, R. H. Friend and F. Deschler, *Nature Communications*, 2015, **6**.
46. Y. Yang, D. P. Ostrowski, R. M. France, K. Zhu, J. van de Lagemaat, J. M. Luther and M. C. Beard, *Nat Photon*, 2015, **10**, 53–59.
47. N. Sestu, M. Cadelano, V. Sarritzu, F. Chen, D. Marongiu, R. Piras, M. Mainas, F. Quochi, M. Saba, A. Mura and G. Bongiovanni, *The Journal of Physical Chemistry Letters*, 2015, **6**, 4566–4572.

## Electronic Supplementary Information

Arman Mahboubi Soufiani<sup>1</sup>, Zhuo Yang<sup>2</sup>, Trevor Young<sup>1</sup>, Atsuhiko Miyata<sup>2</sup>, Alessandro Surrente<sup>2</sup>,  
Alexander Pascoe<sup>3</sup>, Krzysztof Galkowski<sup>2,4</sup>, Roberto Brenes<sup>5</sup>, Joanna Urban<sup>2</sup>, Nan Zhang<sup>2</sup>, Vladimir  
Bulovic<sup>5</sup>, Oliver Portugall<sup>2</sup>, Yi-Bing Cheng<sup>3</sup>, Robin J. Nicholas<sup>6</sup>, Anita Ho-Baillie<sup>1\*</sup>, Martin A. Green<sup>1</sup>,  
Paulina Plochocka<sup>2\*</sup>, Samuel D. Stranks<sup>5,7\*</sup>

<sup>1</sup>Australian Centre for Advanced Photovoltaics,  
School of Photovoltaic and Renewable Energy Engineering,  
University of New South Wales, Sydney, NSW 2052, Australia

<sup>2</sup>Laboratoire National des Champs Magnétiques Intenses, CNRS-UGA-UPS-INSA, 143  
Avenue de Rangueil, 31400 Toulouse, France

<sup>3</sup>Department of Materials Science and Engineering, Monash University, Clayton, Vic 3800, Australia

<sup>4</sup>Institute of Experimental Physics, University of Warsaw - Pasteura 5, 02-093 Warsaw, Poland

<sup>5</sup>Research Laboratory of Electronics, Massachusetts Institute of Technology, Cambridge, MA 02139,  
United States

<sup>6</sup>Clarendon Laboratory, University of Oxford, Parks Road, Oxford OX1 3PU, United Kingdom

<sup>7</sup>Cavendish Laboratory, University of Cambridge, J. J. Thomson Avenue, Cambridge CB3 0HE,  
United Kingdom

\*e-mail:

[a.ho-baillie@unsw.edu.au](mailto:a.ho-baillie@unsw.edu.au)

[paulina.plochocka@lncmi.cnrs.fr](mailto:paulina.plochocka@lncmi.cnrs.fr)

[sds65@cam.ac.uk](mailto:sds65@cam.ac.uk)

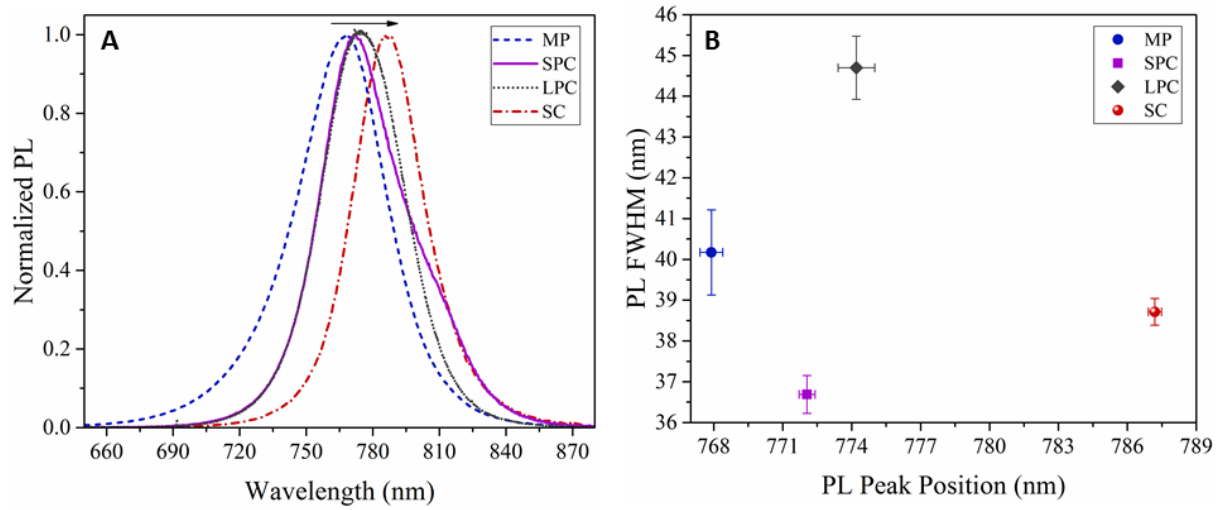


**Figure S1** **A)** Examples of spectral PL measured on the four different  $\text{CH}_3\text{NH}_3\text{PbI}_3$  morphologies used in this study. **B)** Extracted PL peak position and FWHM values from a single pseudo-Voigt profile fit to the spectra of various spots on the four different types of samples presented in **(A)**.

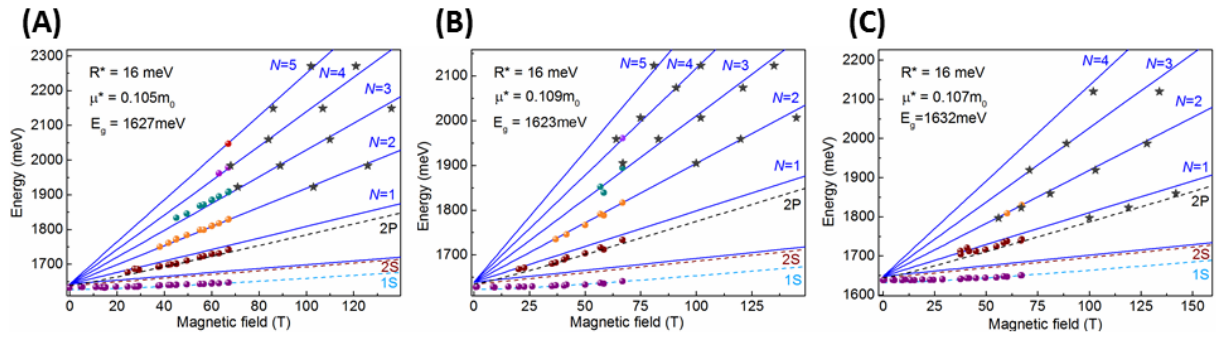


**Figure S2** Fan chart for the small grain polycrystalline (SPC; **A**), small crystal (SC; **B**) and mesoporous (MP; **C**)  $\text{CH}_3\text{NH}_3\text{PbI}_3$  samples. The circular data points are from long pulse filed measurements and star symbol points are collected by short pulse mega-gauss measurements. The solid lines and the dashed lines are the fits to the set of Landau levels and the excitonic transitions, respectively.